JMEPEG (2018) 27:2205–2215
https://doi.org/10.1007/s11665-018-3308-8

1059-9495/$19.00

Composites Strengthened with Graphene Platelets and Formed in Semisolid State Based on α and α/β MgLiAl Alloys

Jan Dutkiewicz, Łukasz Rogal, Przemyslaw Fima, and Piotr Ozga

(Submitted October 17, 2017; in revised form December 20, 2017; published online April 4, 2018)

MgLiAl base composites strengthened with graphene platelets were prepared by semisolid processing of ball-milled alloy chips with 2% of graphene platelets. Composites strengthened with graphene platelets show higher hardness and yield stress than the cast alloys, i.e., 160 MPa as compared to 90 MPa for as-cast alloy MgLi9Al1.5. Mechanical properties for MgLiAl-based composites were similar or higher than for composites based on conventional AZ91 or WE43 alloys. The strengthening however was not only due to the presence of graphene, but also phases resulting from the reaction between carbon and lithium, i.e., Li_2C_2 carbide. Graphene platelets were located at globules boundaries resulting from semisolid processing for all investigated composites. Graphene platelets were in agglomerates forming continuous layers at grain boundaries in the composite based on the alloy MgLi4.5Al1.5. The shape of agglomerates was more complex and wavy in the composite based on MgLi9Al1.5 alloy most probably due to lithium–graphene reaction. Electron diffraction from the two-phase region α + β in MgLi9Al1.5 indicated that [001]α and [110]β directions are rotated about 4° from the ideal relationship [001] hex || [110] bcc phases. It showed higher lattice rotation than in earlier studies what is most probably caused by lattice slip and rotation during semisolid pressing causing substantial deformation particularly within the β phase. Raman spectroscopy studies confirmed the presence of graphene platelets within agglomerates and in addition the presence mainly of Li_2C_2 carbides in composites based on MgLi4.5Al1.5 and Mg9Li1.5Al alloys. From the character of Raman spectra refinement of graphene platelets was found in comparison with their initial size. The graphene areas without carbides contain graphene nanoplatelets with lateral dimension close to initial graphene sample. Electron diffraction allowed to confirm the presence of Li_2C_2 carbide at the surface of agglomerates found from Raman spectroscopy results.

Keywords GNP-strengthened Mg alloy composite, metallic matrix composites, MgLiAl alloys, electron microscopy, semisolid processing

1. Introduction

Composites based on light alloys strengthened with graphene nanoplatelets (GNPs) or carbon nanotubes (CNTs) have been recently investigated in several research articles (Ref 1-10). The graphene and graphene oxide show promise as reinforcements in high-performance nanocomposites. They have a high level of stiffness and strength, and this means that the nanocomposites ought to have outstanding mechanical properties. There are problems, however, in obtaining a good dispersion, and there are challenges in obtaining the full exfoliation of graphene into single- or few-layer material with reasonable lateral dimensions (Ref 1). To improve dispersion of graphene and obtain enhanced mechanical properties of Al matrix graphene-reinforced composites, the magnesium ions were utilized as an "anchor" that made graphene nanosheets attracted to the surface of Al powder (Ref 2). About 20% increase in yield strength with preserved good plasticity was obtained in the AZ31 magnesium alloy strengthened with 1.5-3% of graphene nanoplatelets (GNPs) fabricated by stir-casting method (Ref 3). It was found that, like CNTs, GNPs also have the potential to sustain tensile strength at high temperatures. In another work (Ref 4) graphene nanoplatelets (few-layer graphene) and carbon nanotubes were used as reinforcement fillers to enhance the mechanical properties of AZ31 magnesium alloy through high-energy ball milling, sintering and hot extrusion techniques. The tensile strength of AZ31 magnesium alloy with the graphene nanoplatelet addition decreased by about 11%, while the carbon nanotubes addition brought about 8% increase in the composite tensile strength. The GNPs addition to the AZ61 alloy had also a significant effect on the grain size refinement and change in basal texture due to their uniform distribution throughout the composite matrix, which resulted in considerable improvement of room temperature micro-hardness, tensile and compression strengths (Ref 5). Due to substantial effect of uniform graphene distribution on mechanical properties, novel nanoprocessing methods that combined liquid-state ultrasonic processing and solid-state stirring were applied for the fabrication of bulk metal–graphene nanoplatelet nanocomposites (Ref 6). The obtained Mg-based metal matrix nanocomposite reinforced with graphene nanoplatelets showed a uniform dispersion of graphene nanoplatelets and enhanced properties by 80% as compared with the basic alloy. The good bonding between the graphene nanoplatelets and the Mg matrix facilitates the stress transfer

Jan Dutkiewicz, Łukasz Rogal, Przemyslaw Fima, and **Piotr Ozga**, Institute of Metallurgy and Materials Science of the Polish Academy of Sciences, 25, Reymonta Str, 30-059 Kraków, Poland. Contact e-mail: j.dutkiewicz@imim.pl.

from the Mg matrix to the high-strength graphene nanoplatelets (Ref 7). The studies of GNPs-strengthened composites based on Mg6Zn alloy (Ref 8) showed an increased strength of synthesized composites that could be attributed to the grain refinement, uniform dispersion of GNPs, changes in basal textures and basic strengthening mechanisms. Moreover, the comparison of synthesized composites with Mg6Zn–CNTs composites revealed that GNPs have high potential to replace CNTs because GNPs are 4-6 times cheaper than CNTs (Ref 8). The increase in Al content in the magnesium matrix strengthened with 0.18% GNPs led to increase in YS, UTS and failure strain. The best improvement was achieved at 1 wt.% Al (Mg–1.0Al–0.18GNPs). The mechanical strength of synthesized composites proved to be better than Mg-Al-CNTs and Mg–ceramic composites (Ref 9) which disagrees with the statements of earlier cited works (Ref 4, 5). Nevertheless, in all papers it was reported that the addition of GNPs or CNTs increases the strength and often ductility of composites. Usually MgZnAl alloys were subjected to strengthening using GNPs and CNTs (Ref 3-10) except for the amorphous MgNiLa one (Ref 11), in which the electrochemical characteristics of amorphous Mg65Ni27La8 electrode were improved by the addition of graphene modified with silver nanoparticles. The interfacial reactions were observed in composites based on AZ61 alloy strengthened with carbon nanotubes (Ref 12). The carbide phase Al_2MgC_2 was identified at the interface resulting from such reactions. The composite was effectively strengthened by the production of Al_2MgC_2 compounds at the interface between magnesium matrix and carbon nanotubes.

In the present paper the composites based on MgLiAl alloys consisting either of hexagonal α phase or of hexagonal α + β bcc phase were investigated. Two-phase alloy is of particular interest since it shows very good plasticity attaining superplastic deformation at slightly elevated temperatures (Ref 13, 14). It would be therefore of interest to improve its strength by the addition of GNPs while preserving its good ductility. New procedure, i.e., formation of composite using semisolid processing of milled powders was used to obtain a good dispersion of GNPs in MgLiAl alloys. The presence of lithium in liquid phase in semisolid state of MgLiAl alloys during final formation of composite can favor the reactive wetting of GNPs. Hence, detailed analysis of GNPs, carbides and other compounds at interface will be performed with particular attention to GNP/matrix alloy, where formation of carbides can be expected as reported in (Ref 12).

2. Experimental Procedure

The MgLiAl alloys of composition MgLi9Al1.5 and MgLi4.5Al1.5 (in wt.%) were prepared from pure components: Al (99.999), Li (99.9), Mg (99.99 wt.%). Since the alloy components differed greatly with respect to the melting temperature (Li: 180.5 °C, Mg: 650 °C) as well as density (at room temperature, Li: 0.535 $g{\cdot}cm^{-3}$, Al: 2.7 $g{\cdot}cm^{-3}$), the preparation of alloys was divided into steps. In order to provide protective atmosphere, the furnace was placed in a glove box filled with high-purity argon gas (99.9997%), which circulated in a closed circuit purified with titanium shavings at 850 °C. At this temperature Ti reacts with traces of oxygen, moisture (monitored and kept at a < 0.3 ppm level) and nitrogen, removing them from the glove box. Since liquid lithium easily reacts with graphite and many ceramics, the final, lithium containing ternary alloy was prepared in a molybdenum crucible. The alloys were cut into chips and then milled in planetary mill using hard metal balls and 2 wt.% of graphene platelets (brand name FLRGO) of thickness 6-12 nm supplied by Nanomaterials Company, Warsaw. The high-resolution TEM micrograph of the typical graphene platelet is shown in Fig. 1, where 0002 basal hcp planes of graphite within a plate about 10 nm thick can be seen. The chips were hot pressed at 350 °C what allow to obtain feedstock for thixoforming. The process was conducted using a specially built prototype of a horizontal press (Ref 15). A feedstock was placed inside the coil of an inductive furnace and heated up to 600 °C (at a heating rate of about 70 °C/min), which corresponded to about 30% of the liquid phase, respectively (according to the DSC curve, not presented here). The temperature of the feedstock was measured with an S-type thermocouple. The billet was then moved to the horizontal press sleeve and forced by a piston (velocity 1.5 m/s) into the die cavity in the axial direction at the pressing force of 250 kN. To avoid the surface oxidation effect in the sample, the process was conducted in an Ar atmosphere. The die was made of steel for hot work (HS6-5-2) with a temperature of 20 °C and sprayed with BN. A few thixoformed cuboid shape samples (50 mm × 25 mm × 10 mm) were produced in such a way. The average rate of cooling from the temperature 600 °C to the die temperature was about 110 °C/s. The resulting composite was tested for mechanical properties such as hardness measured using a Zwick/ZHU 250 tester under the load of 5 kg in accordance with ASTM E92. The compression test was performed following PN-57/H-04320 using an INSTRON 3382 machine and samples 3 mm in diameter and 4.5 mm in height. The microstructure was studied using Leica optical and transmission electron Philips CM20 microscopes. Thin samples of the composites were cut with electrospark device, then dimpled and electropolished in an electrolyte consisting of 750 ml AR grade methanol, 150 ml butoxyethanol, 16.74 g magnesium perchlorate and 7.95 g lithium chloride and finally dimpled using Gatan dimpler and ion beam thinned using Leica EM RES101 ion beam thinner.

The Raman spectroscopy is one of the most sensitive techniques to characterize sp^2-hybridized carbon materials

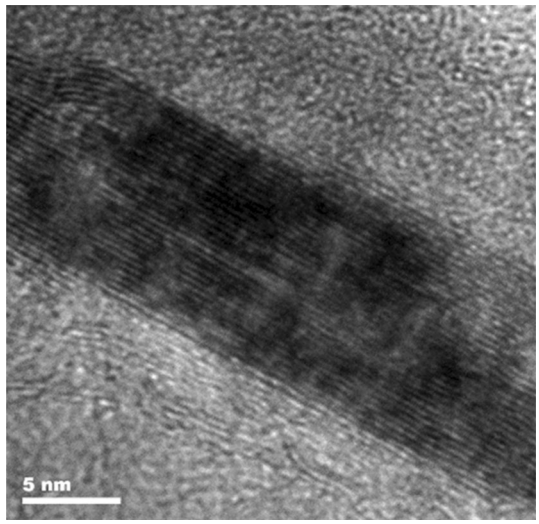

Fig. 1 High-resolution TEM micrograph of the graphene platelet at [010] zone axis orientation

(graphite, graphene, carbon nanotubes (CNTs), etc.) by the analysis of G and 2D band parameters. The characterization of disorder is also possible by the analysis of the D band which is caused by the structure disorder of sp^2-hybridized carbon materials. Hence, Raman spectroscopy can be also very helpful in the analysis of composites containing carbon materials. The micro-Raman spectra were obtained using a Renishaw InVia Raman spectrometer equipped with a Leica optical microscope. The Raman spectra were excited by the 633-nm NeHe laser (1 s exposure time, 14 mW output power) in backscattering geometry using Leica objective 100x (lateral resolution < 1 μm, depth resolution < 1.8 μm). Spectral maps of composites were acquired in point-by-point 2D mode within the scan area of about 20 μm^2 (XY) at 1 μm step size using Renishaw Wire ver. 3.4 software (about 400 spectra).

The spectral maps were collected in three ranges of Raman shifts (fast mode at fixed position of grating for limited wavenumber range): approx. (1) 50-1000 cm^{-1}, (2) 1000-2000 cm^{-1}, (3) 2600-3250 cm^{-1}. The peak parameters: position, i.e., Raman shift (wavenumber), integral intensity and full width at half maximum (FWHM), were determined by fitting each fragment of spectrum after background correction with pseudo-Voigt profile (linear combination of the Gaussian and Lorentzian curves) using Renishaw Wire ver. 3.4 software. The sets of peak parameters were used to create image maps and histograms of the distribution of peak parameters which can characterize heterogeneity of graphene and the remaining compounds in micro-areas (crystallite size, average distance between defects, etc.). The La dimension of graphene nanoplatelets (i.e., average lateral dimension of nanoplatelets) was estimated from the average FWHM values of graphene G band on the basis of Eq 20 presented by Mallet-Ladeira et al. (Ref 16).

3. Results and Discussion

Table 1 shows results of hardness and compression test measurements. The hardness of composite with graphene addition based on alloy Mg4.5Li1.5Al and the as-cast alloy are very similar (near 60 HV), while the hardness of the composite with graphene based on the Mg9Li1.5Al alloy is much higher than that of the as-cast alloy. Similar results are shown by the compression test experiments shown in Fig. 2, in which the composite based on the MgLi9Al1.5 alloy reveals a higher yield strength and ultimate compression strength than that based on the alloy with lower lithium content. The composite shows higher plasticity and higher compression yield strength than the as-cast alloy which was also observed in the case of MgZn6/graphene or AZ61/graphene composites (Ref 5, 8, 10). Obtained hardness and compression yield strength are similar like in the case of conventional magnesium alloys, however slightly lower than observed in the case of AZ61/graphene composites due to lower strength of α + β AlLi alloys.

Table 1 Results of hardness measurement and compression test experiment of as-cast alloys and composites strengthened with graphene platelets

Sample	Hardness, HV	Compressive yield strength, MPa
Mg4.5Li1.5Al	59 ± 1	105
Mg4.5Li1.5Al +2%Gr	58 ± 2	120
Mg9Li1.5Al	61 ± 1	130
Mg9Li1.5Al + 2%Gr	85 ± 1	160

In order to explain the results of mechanical properties, the structure of alloys was investigated using an optical and transmission electron microscopies. Figure 3 shows optical microstructures of both composites. The alloy with 4.5% of lithium shows black layer of graphene agglomerate placed at grain boundaries. The higher density of precipitates was observed predominantly near grain boundaries since they have flown from the melt of higher content of aluminum and lithium than the solid particles. The composite based on the alloy with higher lithium content shows slightly different microstructure. The graphene agglomerates are not continuously distributed at the grain boundaries, and in addition, their boundaries are not as smooth as in the case of the first alloy, but the interface is more developed and wavy. It suggests that some reactions were occurring at the interface.

In order to identify phases in the composite at higher resolution, transmission electron microscopy was applied. Figure 4 shows a dark particle in a bright matrix of the alloy Mg4.5Li1.5Al with 2% graphene. The diffraction pattern taken from the thin edge of the particle reveals continuous rings characteristic for the nanocrystalline structure, however different from that observed in the copper/graphene platelet composite, where it did not react with the matrix (Ref 17). The diffraction pattern from the graphene particle shows only two diffused rings resulting from the nanocrystalline structure. Its *d*-spacing does not fit well to graphite or graphene platelet as shown in the copper/graphene composite. They fit better to 220 and 400 *d*-spacings of the cubic Li_2C_2 phase. The presence of Li_2C_2 phase was also confirmed by Raman spectroscopy, in which results are presented later in this work. The existence of some reflections may result from the epitaxial growth of Li_2C_2 carbide on the graphene platelets of basal plane orientation. The dark field image taken from the diffused first ring reflection allowed the determination of carbide grain size to be between 5 and 20 nm.

Figure 5 shows TEM micrograph taken from the matrix of MgLi9Al1,5 alloy showing elongated α plates of [010] zone axis in β matrix of [1 $\bar{1}$ 1] zone axis. The [001]α and [110]β directions are rotated about 4° from the ideal relationship [001] hex || [110] bcc. Such deviation was also found in earlier study (Ref 31), where deviation of 0.6° from the Burgers relationship was reported and explained by the transformation-induced lattice strains. Much larger rotation is most probably caused by slip and lattice rotation during pressing in a semisolid state, and additional stresses during crystallization at high cooling rate increased due to the addition of aluminum forming additional phases. Diffraction pattern shows diffused reflections toward Debye–Scherrer rings particularly of the β phase (where also high density of dislocations can be seen) supporting this explanation.

Next micrograph from the same composite in Fig. 6 shows graphite-like particle within the β phase as results from the corresponding diffraction pattern. The diffraction from the graphene platelet particle visible in the upper part of the micrograph is identical to that in the case of the alloy with lower Li content (shown in Fig. 4) and suggests also the

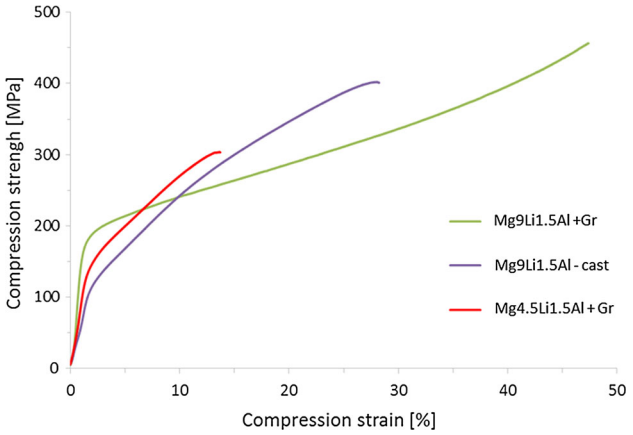

Fig. 2 Compression test curves of as-cast alloy Mg9Li1.5Al and composites strengthened with graphene based on the investigated MgLiAl alloys

formation of lithium carbide Li_2C_2 on the surface of platelets. Probably, due to higher lithium content within the β phase, the formation of carbide is more rapid and the interface is more complex which may cause the increase in mechanical properties due to higher shear stress. However, the expected strength of prepared composites is not as high as reported in AZ61/GNP composites (Ref 5, 8). The reason for lower strength of the investigated composite results most probably from lower mechanical properties of the layer of Li_2C_2 carbide formed at the at the GNP/matrix interface. There are no data in the literature concerning mechanical properties of Li_2C_2 carbide; however, it was characterized as "brittle" (Ref 18) what affects most probably the mechanical properties of prepared composites.

Figure 7 shows the typical bands which were observed in Raman spectra of the composites (marked with black arrows) in fragments of each analyzed range of Raman shift:

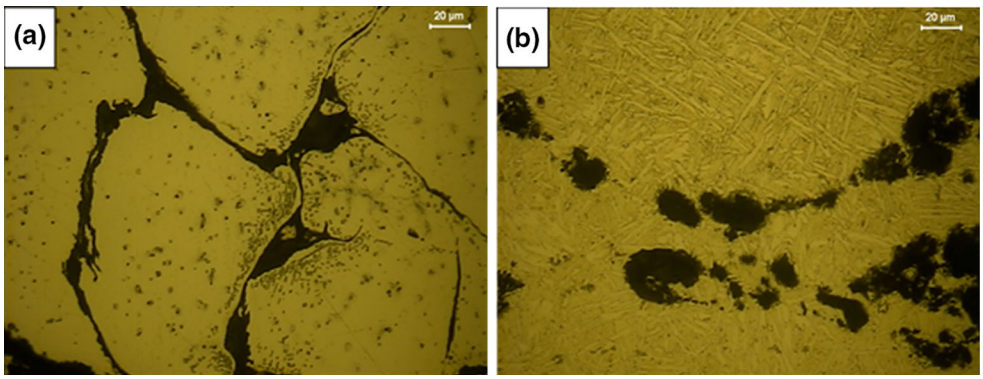

Fig. 3 Optical micrographs of composite based on the MgLi4.5Al1.5 alloy (a) and Mg9Li1.5Al (b) both with 2% graphene and after casting from the semisolid state

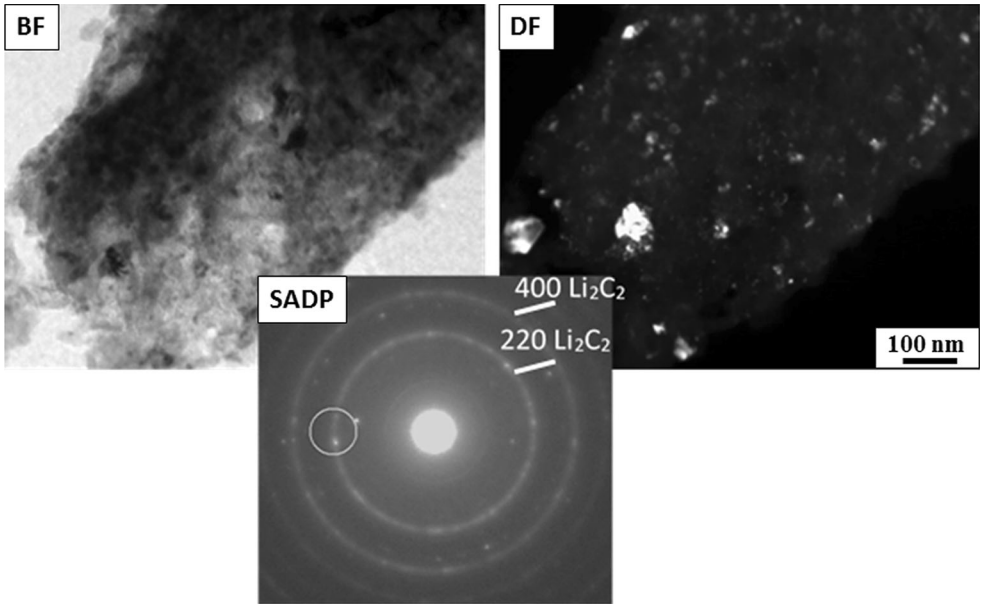

Fig. 4 TEM micrograph in bright field (left side) and dark field (right side) and SADP (selected area diffraction pattern) (below) from the graphene particle in the matrix of alloy Mg4.5Li1.5Al with 2% graphene

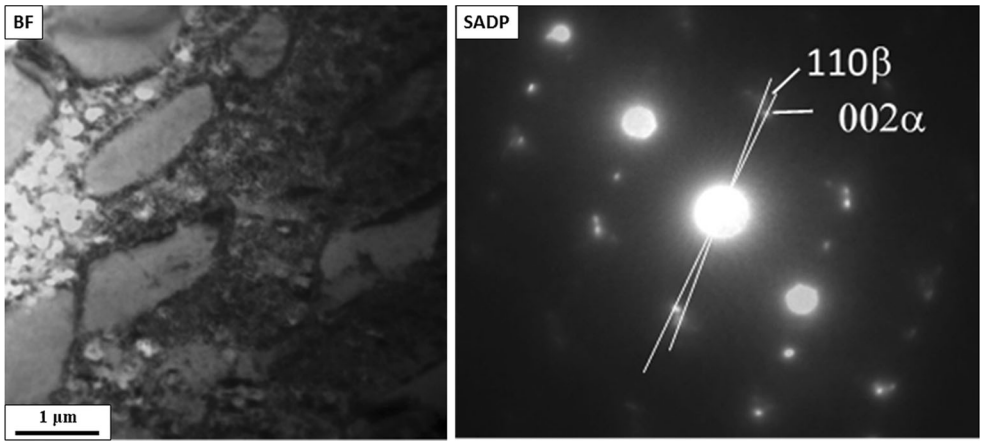

Fig. 5 TEM micrograph from Mg9Li1.5Al1 matrix showing elongated α plates of [010] zone axis in the β matrix of [111] zone axis

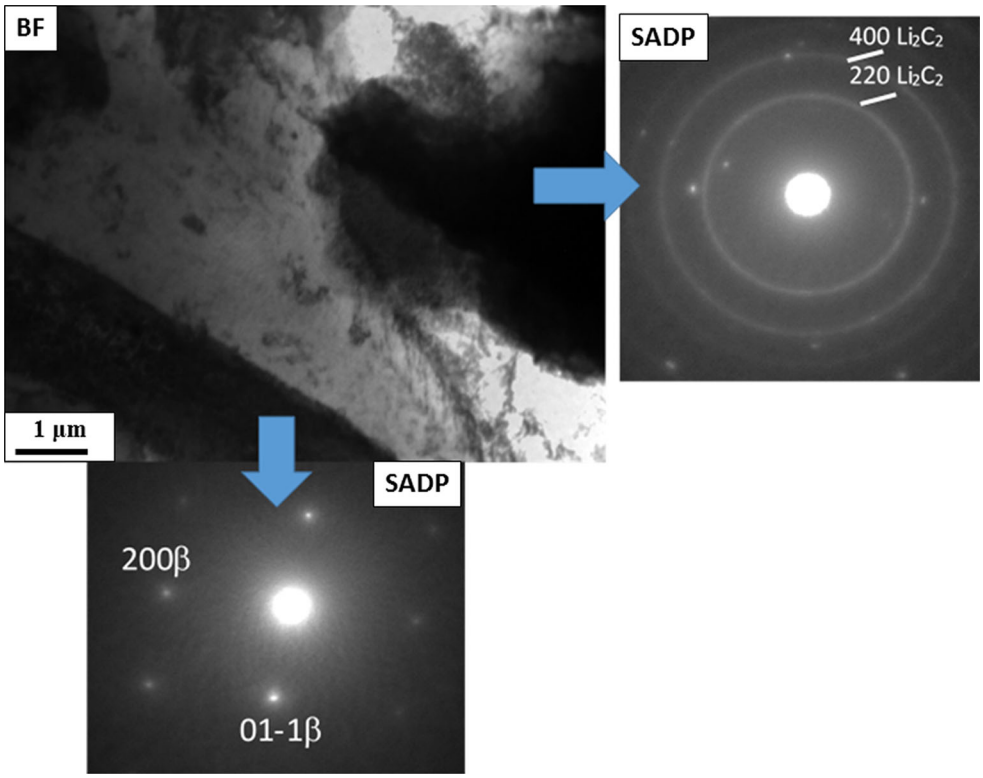

Fig. 6 TEM micrograph of composite based on Mg9Li1.5Al alloy and strengthened with graphene platelets. SADP on the right shows a ring from the surface nanocrystalline layer of Li_2C_2 carbide and single reflections from nanocrystalline graphite phase; diffraction pattern from the dark β plate of [011] zone axis on the left side

1. The range of bands for metallic magnesium phase [E_2g band for hcp Mg (Ref 19)], salt-like carbides, which contain anion C^{4-} (methanides) aluminum and aluminum-magnesium carbides (Al_4C_3, Al_2MgC_2) or anion C_3^{4-} (allylenides) lithium and magnesium carbides (Li_4C_3, Mg_2C_3) (Ref 18) and metal oxides (approx. 50-1000 cm^{-1}),
2. The range of graphene bands D, D' and G, amorphous carbon band (Ref 20), main bands of salt-like carbides, which contain anion C_2^{2-} (acetylides with triple C ≡ C bonds: Li_2C_2, MgC_2 or ternary $(Li,Mg)C_2$) and allylenides (double C=C bonds of allylenides) (Ref 21) and also main band of carbonates (Li_2CO_3, $MgCO_3$) (approx. 1000-2000 cm^{-1}),
3. The range of the 2D band of graphene (Ref 19) (2600-3250 cm^{-1}).

The main bands of Al_4C_3 as also other methanides (Al_2MgC_2), allylenides (Mg_2C_3, Li_4C_3) and oxides were not visible in the spectra of both types of composites. [Red arrows indicate suitable wavenumber positions of Al_4C_3 bands in Fig. 8 on the basis of work (Ref 22).]

Figure 8 indicates that in Mg4.5Li1.5Al composite there can be two types of carbides, which contain anion C_2^{2-} (acetylides) with average Raman shift band positions 1851 cm^{-1} (Fig. 8a) and 1879 cm^{-1} (Fig. 8b), respectively. Similar band positions

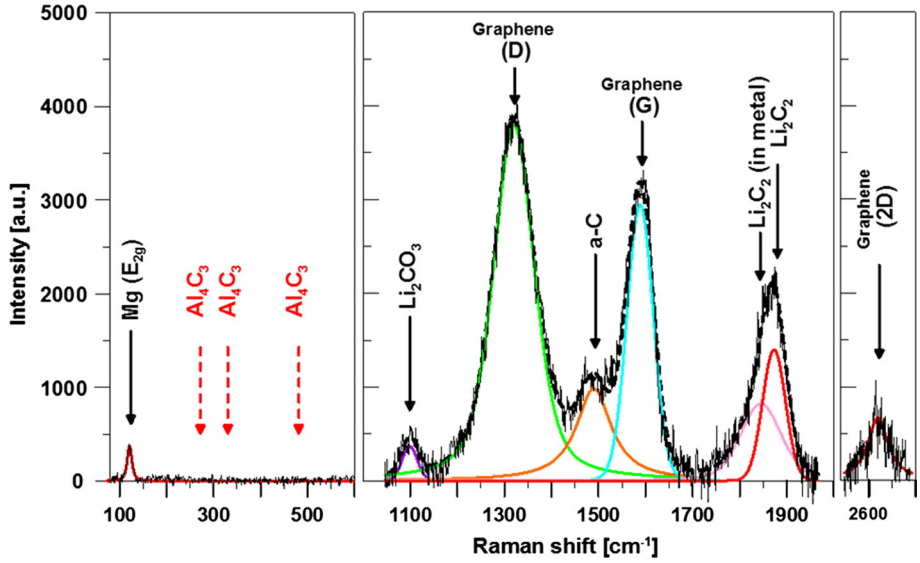

Fig. 7 Typical bands observed in Raman spectra of the composites [black fine line represents the original experimental spectrum, black dotted line represents the fitted spectrum, solid (color) lines represent the fitted model bands, red arrows indicate wavenumber positions of main bands of Al_4C_3 which are absent from spectra of the composites (Ref 2)] (Color figure online)

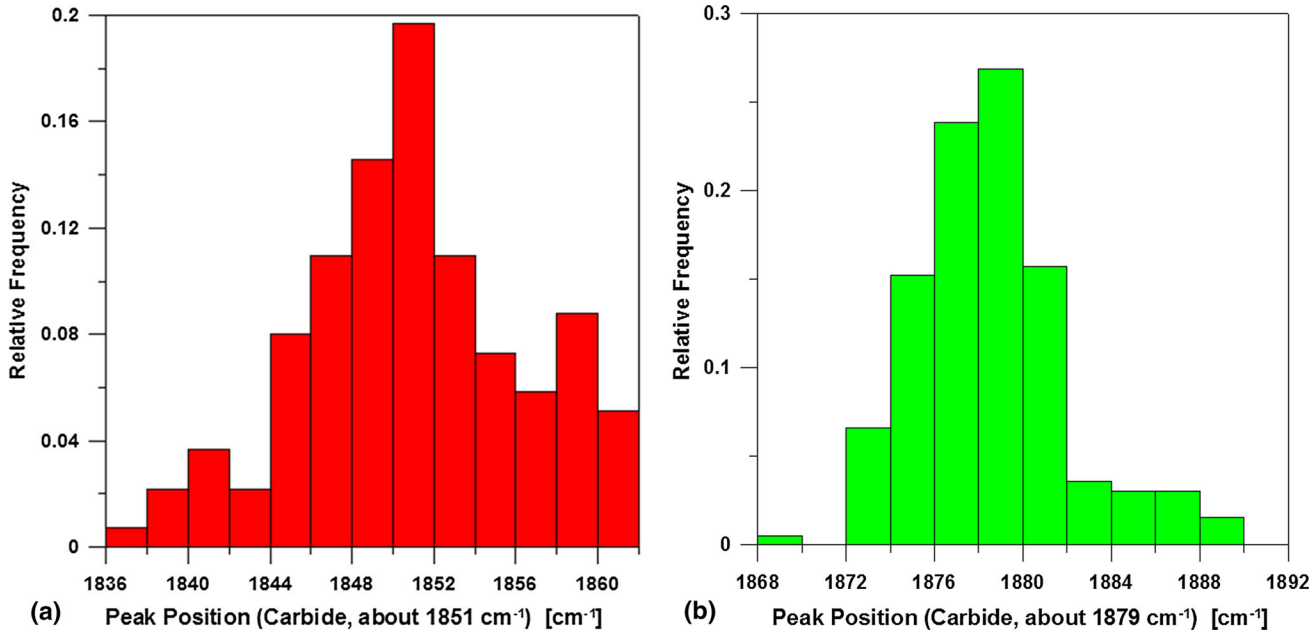

Fig. 8 Peak position distribution histograms in the composite based on Mg4.5Li1.5Al alloy: (a) band of lithium carbide (Li_2C_2) embedded in alloy (1851 cm^{-1}), (b) band of lithium carbide (Li_2C_2) phase (1879 cm^{-1})

of Raman shift were described by Schmitz et al. (Ref 23), and they assigned these bands to two kinds of Li_2C_2 carbides. The Raman shift of the acetylide anion's symmetric stretching mode was found at around 1877 cm^{-1} for the synthesized Li_2C_2 (Ref 23). Similar band wavenumber positions for Li_2C_2 bulk materials are also described by other authors [(Ref 18, 22)—1872 cm^{-1} (Ref 24)—1874 cm^{-1}]. The wavenumber position of this band is also similar in case of nanocrystal and amorphous Li_2C_2 materials (Ref 23). The second kind of Li_2C_2 carbides contains destabilized triple bond of the acetylide by charge transfer from the metal to the acetylide anion of Li_2C_2 (carbide embedded in metal). Schmitz et al. (Ref 23) explained that this effect is responsible for distinct shift of position of Raman band of acetylide anion in Li_2C_2 to 1845 cm^{-1}. The MgC_2 carbide contains also acetylide anion. This carbide can be formed from magnesium and acetylene (Ref 25, 26). The presence of carbide MgC_2 has been reported also in a carbon fiber-reinforced pure Mg composite, but these results were not confirmed in the investigation of Viala et al. (Ref 27). Hence, MgC_2 is probably not formed directly from carbon and magnesium reaction (Ref 24). The tetragonal MgC_2 (space group P42/mnm) is stable to the temperatures as high as 485-500 °C and next decomposes into hexagonal Mg_2C_3 with carbon and above 675-700 °C Mg_2C_3 decomposes into Mg and

amorphous carbon (Ref 25, 27). The Raman spectra of Mg4.5Li1.5Al/GNPs and Mg9Li1.5Al/GNPs composites do not confirm the presence of a significant quantity of Mg_2C_3. (Strong band of the symmetric stretching mode of double C=C bonds of allylenides about 1200 cm^{-1} is absent (Ref 25).) The formation of the ternary carbide Al_2MgC_2 was reported in Mg alloys in some Al and temperature ranges (Ref 14, 28), as also the interfaces which were devoid of carbide reaction products were reported [perhaps due to the passivating effect of the fine-grained crystalline MgO layer that existed in the composites (Ref 27, 29)]. Tentative representation of the Al-C-Mg phase equilibria below 1000 K presented by Viala et al. (Ref 28, Fig. 9) indicates that Al_2MgC_2 carbide should be also present in boundary MgAl/C composites at 600 °C for analyzed Mg to Al ratios; hence, the presence of lithium in MgLiAl/GNPs composites prefers the formation of Li_2C_2 instead of Al_2MgC_2 carbide. Some shifts of band for both types of Li_2C_2 carbides can also indicate the presence of ternary lithium-magnesium carbides (acetylides). In case of MgAl/GNPs composites, none Raman bands are visible from magnesium carbides in acetylide range of wavenumbers (1700-1800 cm^{-1}) (Ref 4, 10).

The optical microstructures containing a fragment with mapping of integral intensities of graphene bands (Fig. 9a) and both types of carbides bands (Fig. 9b) of the composite based on the Mg4.5Li1.5Al alloy strengthened with 2% graphene platelets are shown in Fig. 9. The micrographs are similar to that in Fig. 4a showing graphene platelet conglomerates at the grain boundaries (Fig. 9a) visible however in better contrast as black and white layers. A very wide Raman band of lithium carbides with average FWHM about 41 cm^{-1} indicates the nanocrystalline form of Li_2C_2 (Fig. 10a). Lithium can also be present between graphene layers in platelets causing the formation of carbide Li_xC_6. Such a process of lithium intercalation into carbon was observed in a typical Li-ion battery electrolyte (Ref 30). It causes the shift of Raman G band of GNPs toward higher frequencies even to 1600 cm^{-1} and that of 2D toward lower frequencies even to 2610 cm^{-1}. The observed shift of G band (about 1587 cm^{-1}, Fig. 11a) is not

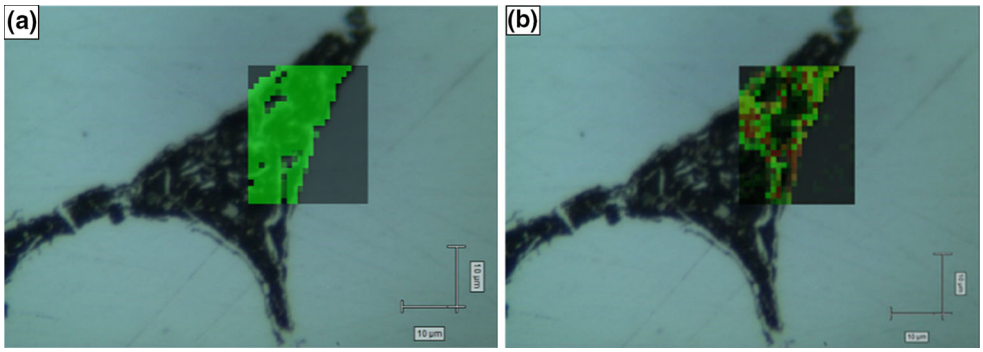

Fig. 9 Optical microstructures of Mg4.5Li1.5Al composite with mapping of integral intensities of bands: (a) graphene (band G, shown in green color); (b) Li_2C_2 carbide embedded in alloy (red) and Li_2C_2 carbide phase (green) (Color figure online)

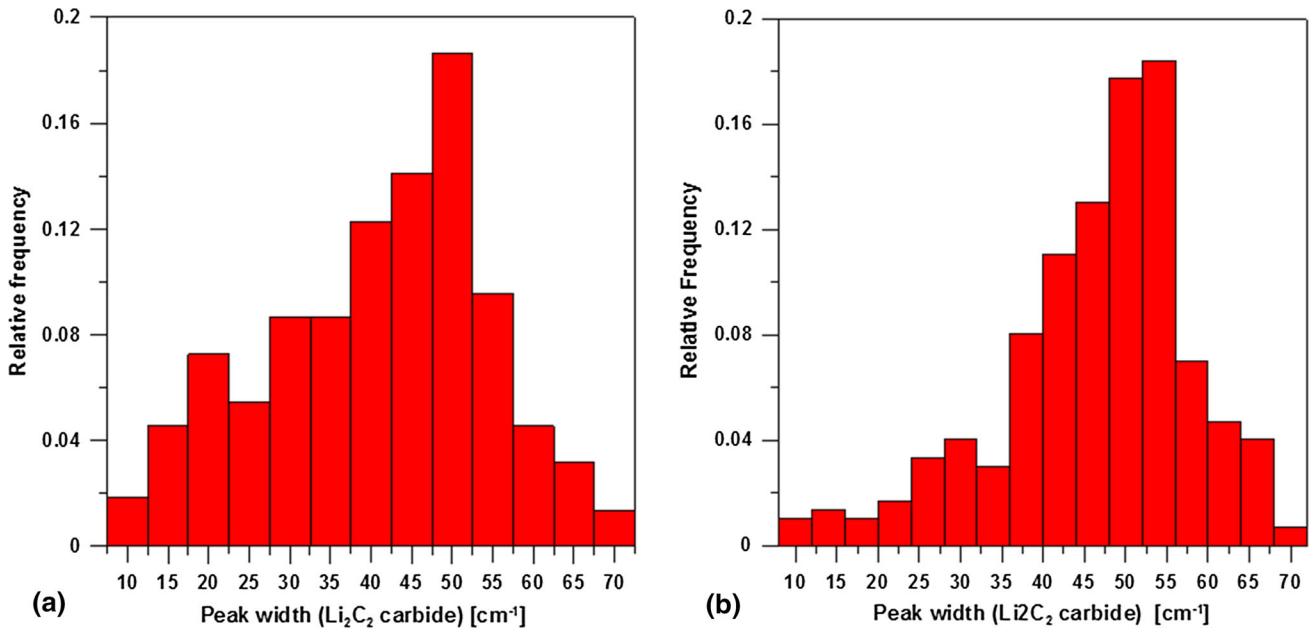

Fig. 10 Distribution histograms of FWHM of lithium carbide (Li_2C_2) phase band: (a) in composite based on Mg4.5Li1.5Al alloy; (b) in composite based on Mg9Li1.5Al alloy

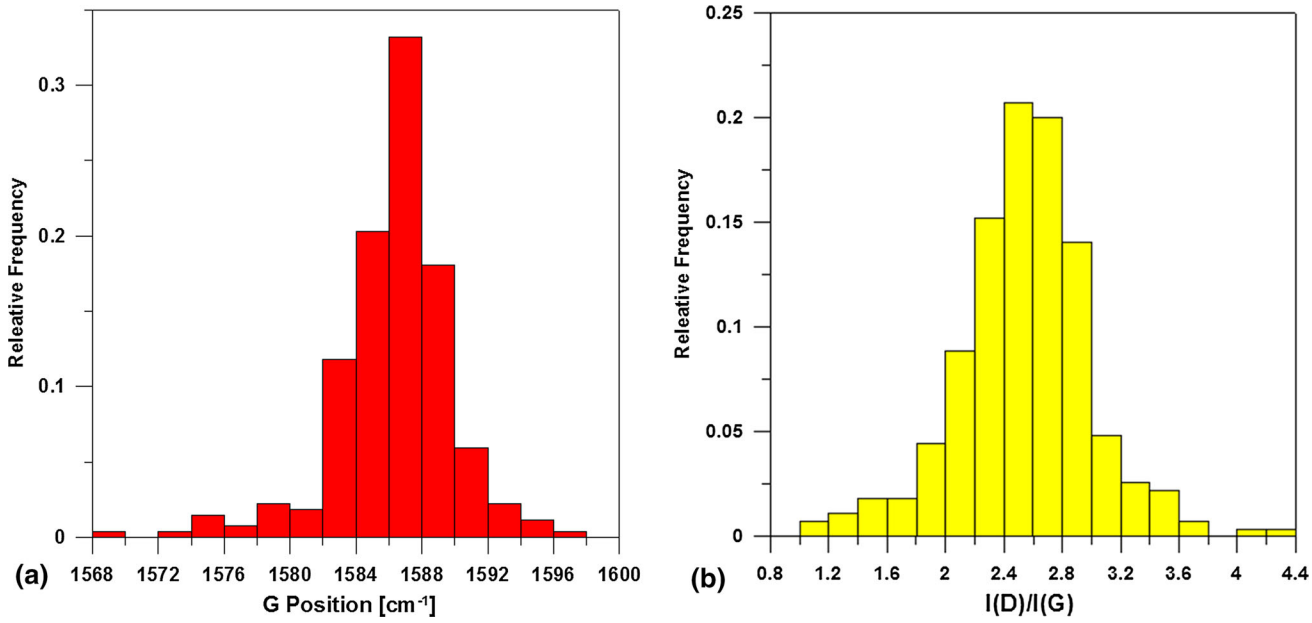

Fig. 11 Distribution histograms in the composite based on Mg4.5Li1.5Al alloy: (a) graphene G band position, (b) ratio of intensities of D to G graphene bands (I(D)/I(G))

very large, but corresponds to that observed during the graphite lithiation and delithiation in the lithium-ion battery electrolyte (Ref 30). It indicates that part of lithium can also be intercalated between graphene layers. The ratios of intensities of D to G band of graphene (average I(D)/I(G)≈2.6) and 2D to G band (I(2D)/I(G)≈0.3) are close to the ratios for the initial graphene sample (I(D)/I(G)≈2.31-2.41 and I(2D)/I(G)≈0.12-1.02); hence, the formation of carbides at the grain boundaries during synthesis of composite based on the Mg4.5Li1.5Al alloy changed the defect density and size of nanoplatelets of graphene only a little. A small increase in average L_a size of graphene nanoplatelets from 6.3 to 7.1 nm can indicate that fine graphene nanoplatelets are more reactive and they form carbides in the first instance. The Raman band E_g of magnesium HCP phase is very weak in Mg4.5Li1.5Al composite, but it is observed in all points of the examined area with similar FWHM (about 12 cm^{-1}), which indicates that there is no change in crystal size of magnesium hcp phase at the grain boundaries. However, change of wavenumber position of magnesium E_g band from the typical Raman shift position 122 cm^{-1} (Ref 31) (light areas in Fig. 10) to 117-119 cm^{-1} at the grain boundaries (dark areas in Fig. 10) was observed. These changes of E_g band wavenumber position at the grain boundary can be the result of greater content of lithium in the magnesium hcp phase, or it can come from stresses of the magnesium phase, brought about by the formation of carbide layer on its surface. In the case of Mg9Li1.5Al/GNPs composite none signal from magnesium E_{2g} band at the grain boundary was observed.

The composite with greater content of lithium shows only one band for the Li_2C_2 carbide with average Raman band wavenumber position about 1873 cm^{-1} (Fig. 12) and a finer size of nanocrystalline Li_2C_2 (increase in average FWHM value from 41 to 46.3 cm^{-1} shown in Fig. 10a and b, respectively). Presence of only Li_2C_2 carbide phase and the lack of both, i.e., second type of lithium carbide (Li_2C_2 embedded in particles of alloys) as also magnesium phase at the grain boundary is the

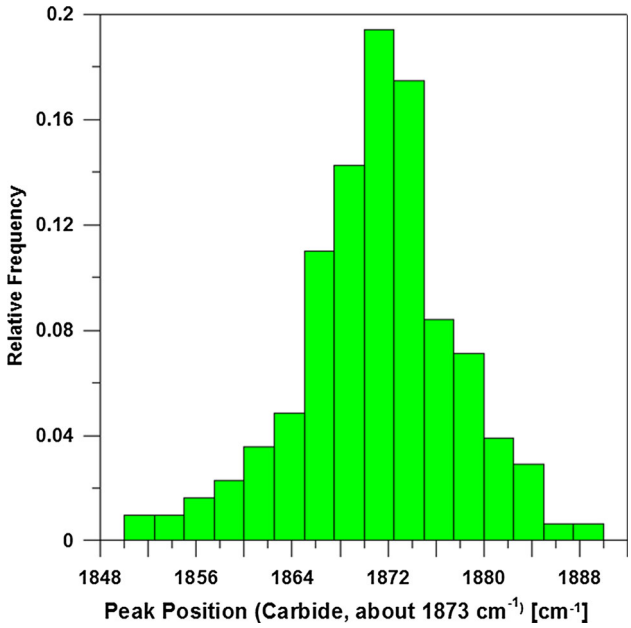

Fig. 12 Peak position distribution histograms of lithium carbide (Li_2C_2) phase band in the composite based on the Mg9Li1.5Al alloy

results of the greater content of lithium in Mg9Li1.5Al/GNPs composite and substantially higher content of lithium in liquid phase in semisolid state of Mg9Li1.5Al alloy during composite formation at 600 °C. U. Ruschewitz and R. Pottgen described structural phase transition in atmospheric pressure in Li_2C_2 between LT (low temperature) modification (orthorhombic, Immm, α-Li_2C_2) and HT (high temperature) modification (cubic, Fm-3m, β-Li_2C_2) (Ref 32). The structural transition does not change acetylides structure (presence of anion C_2^{2-}) of carbide at atmospheric pressure (Ref 33), but He et al. show that in a certain low temperature range, the β-Li_2C_2

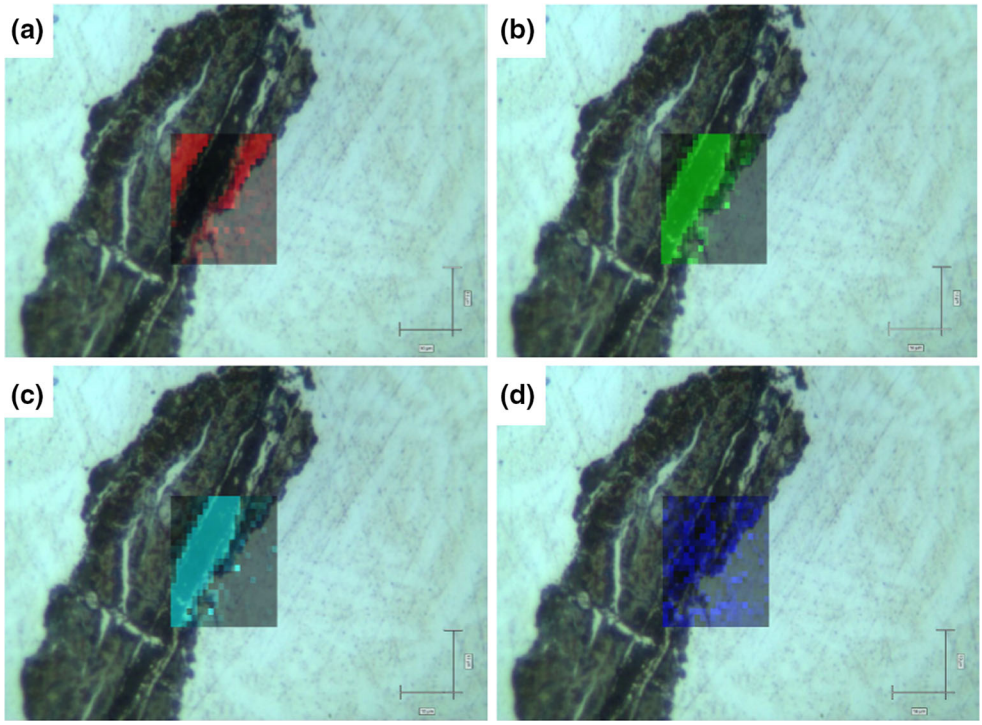

Fig. 13 Optical microstructures of composite Mg9Li1.5Al with mapping of integral intensities of bands: (a) Li_2C_2 phase band (based on the Raman band about 1873 cm^{-1}, shown in red color); (b) graphene band G (shown in green); (c) graphene band D (blue); (d) lithium carbonate—Li_2CO_3 (based on the Raman band about 1087 cm^{-1} in navy blue, Ref 34) (Color figure online)

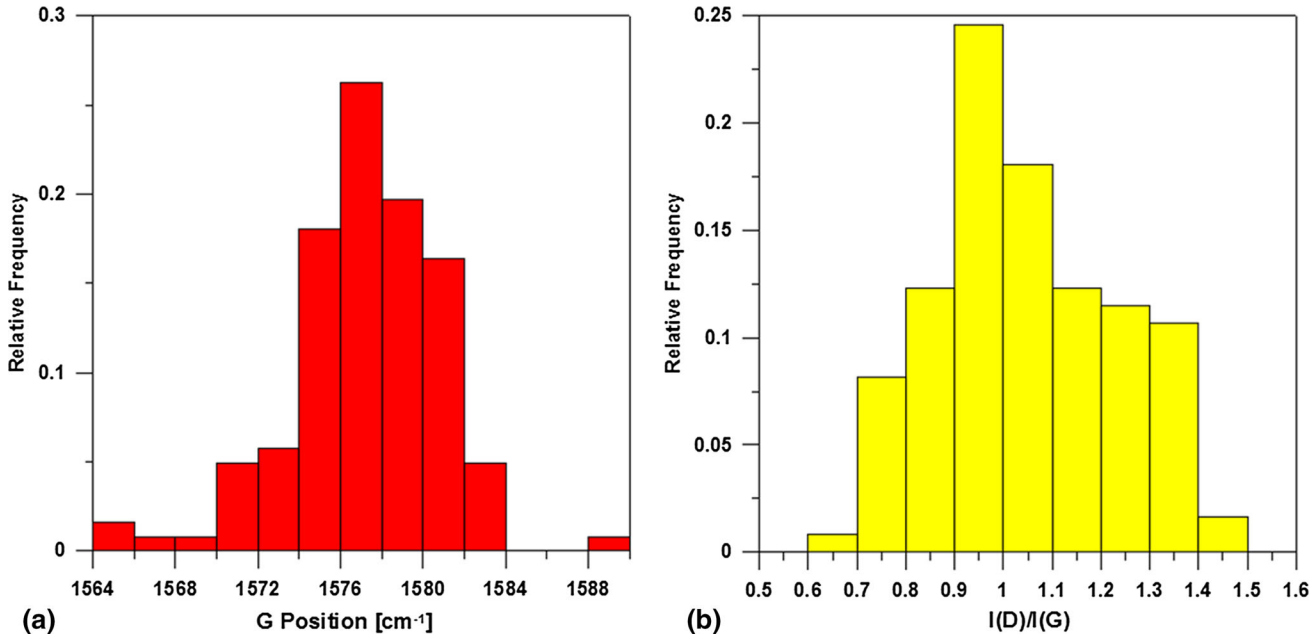

Fig. 14 The distribution histograms in the composite based on the Mg9Li1.5Al alloy: (a) graphene G band wavenumber position, (b) ratio of D to G graphene band intensities (I(D)/I(G))

(metastable phase in the coarse-grained polycrystalline system) can be stabilized due to the nanograin size effect. Hence, at room temperature cubic β-Li_2C_2 can stable for the grain size about 5 nm. This result is confirmed by electron diffraction (Fig. 6 and 8).

Figure 13 shows additionally the optical microstructures with mappings of: (a) lithium carbide (Li_2C_2) based on the integral intensity of Raman band about 1873 cm^{-1} (Fig. 13a, red color), (b) graphene based on the integral intensity of Raman band G, about 1580 cm^{-1} (Fig. 13b, in green), (c) defected graphene based on the integral intensity of band D, about 1330 cm^{-1} (Fig. 13c, blue). The displacement of compounds indicates that lithium carbides are formed in the area between graphene and magnesium phases (Fig. 13a).

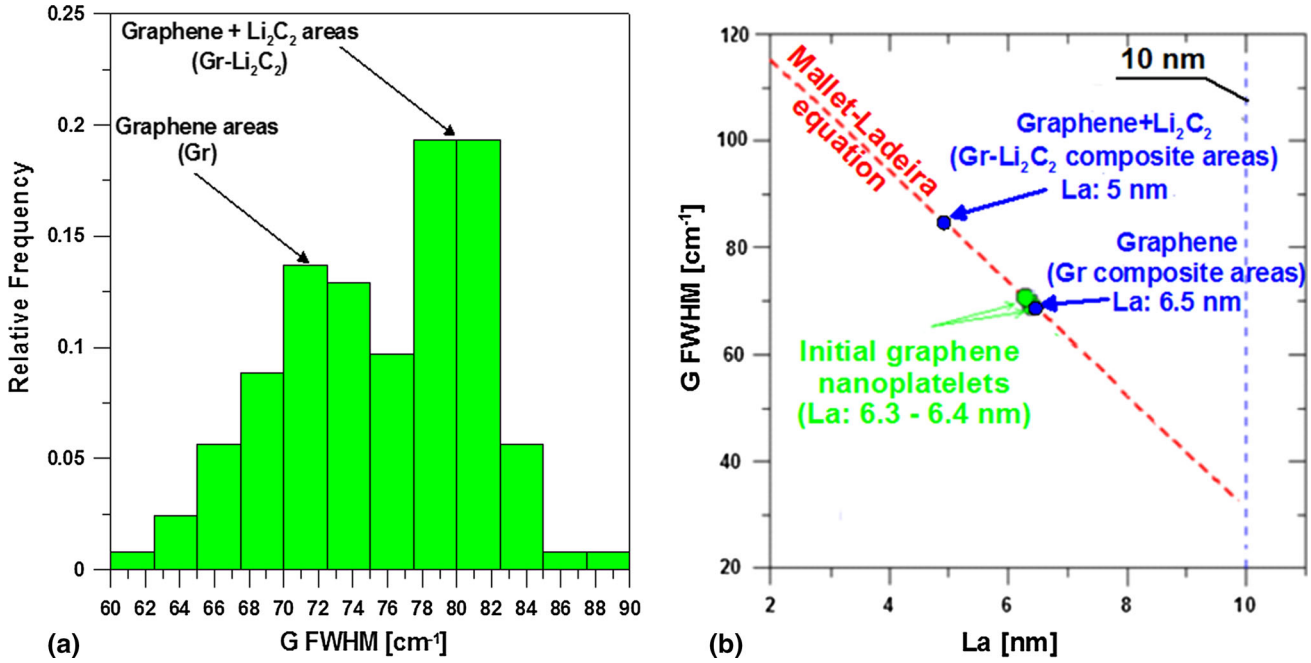

Fig. 15 (a) The bimodal distribution histograms of graphene FWHM G band in the composite based on the Mg9Li1.5Al alloy; (b) dimension of nanoplatelet in graphene areas (Gr) and in graphene-carbide areas (Gr + Li_2C_2) [estimated based on Mallet–Ladeira equation (Ref 16)]

The graphene areas in Mg9Li1.5Al/GNPs composite do not contain intercalated lithium (average wavenumber position of G band about 1578 cm^{-1}, Fig. 14a). The properties of graphene in the graphene-carbides areas are different from these in graphene areas (Fig. 13b and c). Figure 15(a) shows a bimodal distribution of graphene FWHM G band. The first maximum (FWHM about 70 cm^{-1}, Fig. 15a) is connected with graphene nanoplatelets inside the graphene areas which do not contain the carbides. The estimated dimension of nanoplatelets in these areas is close to these in the initial sample of graphene (about 6.5 nm, Fig. 15b). The second maximum (FWHM about 80 cm^{-1}, Fig. 15a) is connected with the graphene nanoplatelets inside the graphene-carbides areas. The estimated dimension of graphene nanoplatelets in these areas is smaller than in graphene areas (about 5 nm, Fig. 15b). These results indicate to the decrease in dimension of graphene nanoplatelets in the result of reaction with lithium. The average ratio I(D)/I(G) close to 1 (Fig. 15b) confirms this conclusion [decrease in I(D)/I(G) ratio from left side of maximum in the Tuinstra–Koenig relation between La and I(D)/I(G) ratio (Ref 20, 35)].

4. Conclusions

1. Composites based on MgLiAl alloys strengthened with graphene platelets were prepared from ball-milled alloy chips and graphene platelets using pressure casting from semisolid range at about 30% of liquid phase. Composites strengthened with 2% of graphene platelets showed higher hardness and compression yield stress of 160 MPa compared with 90 MPa for Mg9Li1.5Al as-cast alloy. Mechanical properties for MgLiAl-based composites were similar to those of conventional magnesium alloys. The increase in strength of MgLiAl/GNP composites was limited due to the formation of a Li_2C_2 brittle layer at graphene platelets interfaces.
2. Graphene platelets were located at boundaries of globules resulting from semisolid processing of all investigated composites. Graphene platelets appeared in agglomerates forming continuous layers at grain boundaries in the composite based on Mg4.5Li1.5Al alloy. Shape of agglomerates was more round in the composite based on Mg9Li1.5Al alloy. Electron diffraction from two-phase region in Mg9Li1.5Al indicated that [001]α and [110]β directions rotated about 4° from the ideal relationship [001] hex || [110] bcc phases. It confirmed the earlier study of (Ref 17), and slightly larger rotation might be caused by the increased transformation stresses due to the addition of aluminum.
3. Raman spectroscopy studies confirmed the presence of graphene platelets within agglomerates and the presence of Li_2C_2 carbides in composites based on Mg4.5Li1.5Al and Mg9Li1.5Al alloys. Refinement of graphene platelets in graphene-carbides areas was observed from the character of Raman spectra in comparison with the initial graphene platelets. Graphene areas without carbides contained graphene nanoplatelets with average lateral dimension (L_a) close to initial graphene sample. Electron diffraction confirmed the presence of Li_2C_2 carbide at surface of agglomerates in accordance with Raman spectroscopy results. Composites with lower lithium content (based on Mg4.5Li1.5Al) also contained Li_2C_2 carbide but embedded in alloy particles at the grain boundary.
4. Based on results for MgLiAl-based composites strengthened with graphene platelets prepared by semisolid casting, a moderate increase in strength was attained accompanied by improved plasticity for the two-phase α + β alloys. Strengthening however was not only due to the presence of graphene, but also to the occurrence of phases originated from the reaction between carbon and lithium in the form of Li_2C_2 carbide.

Acknowledgments

The financial support of the National Science Center (NCN) under Project Number 2014/15/B/ST8/03184 and the Polish National Centre for Research and Development, Grant No.: LIDER/007/151/L-5/13/NCBR/2014, is gratefully acknowledged.

References

1. R.J. Young, I.A. Kinloch, L. Gong, and K.S. Novoselov, The Mechanics of Graphene Nanocomposites: A Review, *Compos. Sci Technol.*, 2012, **72**, p 1459–1476
2. J.M. Ju, G. Wang, and K.H. Sim, Facile Synthesis of Graphene Reinforced Al Matrix Composites with Improved Dispersion of Graphene and Enhanced Mechanical Properties, *J. Alloy. Compd.*, 2017, **704**, p 585–592
3. M. Rashad, F. Pan, Y. Liu, X. Chen, H. Lin, R. Pan, M. Asif, and J. She, High Temperature Formability of Graphene Nanoplatelets-AZ31 Composites Fabricated by Stir-Casting Method, *J. Magnes. Alloys*, 2016, **4**, p 270–277
4. M. Rashad, F. Pan, J. Zhang, and M. Asif, Use of High Energy Ball Milling to Study the Role of Graphene Nanoplatelets and Carbon Nanotubes Reinforced Magnesium Alloy, *J. Alloy. Compd.*, 2015, **646**, p 223–232
5. M. Rashad, F. Pan, D. Lin, and M. Asif, High Temperature Mechanical Behavior of AZ61 Magnesium Alloy Reinforced with Graphene Nanoplatelets, *Mater. Des.*, 2016, **89**, p 1242–1250
6. L.-Y. Chen, H. Konishi, A. Fehrenbacher, Ch Ma, J.Q. Xu, H. Choi, H.F. Xu, F.E. Pfefferkorn, and XCh Li, Novel Nanoprocessing Route for Bulk Graphene Nanoplatelets Reinforced Metal Matrix Nanocomposites, *Scripta Mater.*, 2012, **67**, p 29–32
7. R.D. Evans, M.W. Phaneuf, and J.D. Boyd, Imaging Damage Evolution in a Small Particle Metal Matrix Composite, *J. Microsc.*, 1999, **196**, p 146
8. M. Rashad, F. Pan, and M. Asif, Exploring Mechanical Behavior of Mg–6Zn Alloy Reinforced with Graphene Nanoplatelets, *Mater. Sci. Eng. A*, 2016, **649**, p 263–269
9. M. Rashad, F. Pan, A. Tang, M. Asif, S. Hussain, J. Gou, and J. Mao, Improved strength and Ductility of Magnesium with Addition of Aluminum and Graphene Nanoplatelets (Al + GNPs) Using Semi Powder Metallurgy Method, *J. Ind. Eng. Chem.*, 2015, **23**, p 243–250
10. M. Rashad, F. Pan, H. Hua, M. Asif, S. Hussain, and J. She, Enhanced Tensile Properties of Magnesium Composites Reinforced with Graphene Nanoplatelets, *Mater. Sci. Eng. A*, 2015, **630**, p 36–44
11. L.J. Huang, Y.X. Wang, J.-G. Tang, Y. Wang, J.X. Liu, Z. Huang, J.Q. Jiao, W. Wang, M.J. Kipper, and L.A. Belfiroe, A New Graphene Nanocomposite to Improve the Electrochemical Properties of Magnesium-Based Amorphous Alloy, *Mater. Lett.*, 2015, **160**, p 104–108
12. H. Fukuda, K. Kondoh, J. Umeda, and B. Fugetsu, Interfacial Analysis Between Mg Matrix and Carbon Nanotubes in Mg–6 wt.% Al Alloy Matrix Composites Reinforced with Carbon Nanotubes, *Comput. Sci Technol.*, 2011, **71**, p 705–709
13. M. Furui, Ch Xu, T. Aida, M. Inoue, H. Anada, and T.G. Langdon, Improving the Superplastic Properties of a Two-Phase Mg–8%Li Alloy Through Processing by ECAP, *Mater. Sci. Eng. A*, 2005, **410–411**, p 439–442
14. F. Cao, F. Xia, and G. Xue, Hot Tensile Deformation Behavior and Microstructural Evolution of a Mg–9.3Li–1.79Al–1.61Zn Alloy, *Mater. Des.*, 2016, **92**, p 44–57
15. Ł. Rogal, J. Dutkiewicz, T. Czeppe, J.T. Bonarski, and B. Olszowska-Sobieraj, Characteristics of 100Cr6 Bearing Steel After Thixoforming Process Performed with Prototype Device, *Trans. Nonferrous Met. Soc. China*, 2010, **20**, p 1033–1036
16. P. Mallet-Ladeira, P. Puech, C. Toulouse, M. Cazayous, N. Ratel-Ramond, P. Weisbecker, G.L. Vignoles, and M. Monthioux, A Raman Study to Obtain Crystallite Size of Carbon Materials: A Better Alternative to the Tuinstra–Koenig Law, *Carbon*, 2014, **80**, p 629–639
17. J. Dutkiewicz, W. Maziarz, P. Ozga, J. Pstruś, B. Kania, P. Bobrowski, and J. Stolarska, Microstructure and Properties of Bulk Copper Matrix Composites Strengthened with Various Kinds of Graphene Nanoplatelets, *Mater. Sci. Eng. A*, 2015, **628**, p 124–134
18. M. V. Alenina, V. P. Kolotov, Yu. M. Platov, Lithium Carbide is Prospective Material for Breeder of Fusion Reactor, *Perspektivnye Materialy, 2013,* No. 7, pp. 44–48 (**in Russian**)
19. A.F.E. Goncharov, V.V. Gregoryanz, R.J. Struzhkin, H.K. Hemley, N. Mao, N. Boctor, E. Huang, Raman scattering of metals to very high pressures, *High Pressure Phenomena*, R.J. Hemley et al., Ed., IOS Press/Società Italiana di Fisica, Amsterdam, 2002, p 297–313
20. A.C. Ferrari, Raman Spectroscopy of Graphene and Graphite: Disorder, Electron–Phonon Coupling, Doping and Nonadiabatic Effects, *Solid State Commun.*, 2007, **143**, p 47–57
21. U. Ruschewitz, Binary and Ternary Carbides of Alkali and Alkaline-Earth Metals, *Coord. Chem. Rev.*, 2003, **244**, p 115–136
22. Y. Sun, H. Cui, L. Gong, J. Chen, P.K. Shen, and C.X. Wang, Field Nanoemitter: One-Dimension Al_4C_3 Ceramics, *Nanoscale*, 2011, **3**, p 2978
23. R. Schmitz, R. Müller, S. Krüger, R.W. Schmitz, S. Nowak, S. Passerini, M. Winter, and C. Schreiner, Investigation of Lithium Carbide Contamination in Battery Grade Lithium Metal, *J. Power Sources*, 2012, **217**, p 98–101
24. C. Naudin, J.L. Bruneel, M. Chami, B. Desbat, J. Grondin, J.C. Lassègues, and L. Servant, Characterization of the Lithium Surface by Infrared and Raman Spectroscopies, *J. Power Sources*, 2003, **124**, p 518–525
25. T.A. Strobel, O.O. Kurakevych, D.Y. Kim, Y. Le Godec, W. Crichton, J. Guignard, N. Guignot, G.D. Cody, and A.R. Oganov, Synthesis of β-Mg2C3: A Monoclinic High-Pressure Polymorph of Magnesium Sesquicarbide, *Inorg. Chem.*, 2014, **53**, p 7020–7027
26. P. Karena, A. Kjekshusa, Q. Huang, and V.L. Karen, The Crystal Structure of Magnesium Dicarbide, *J. Alloy. Compd.*, 1999, **282**, p 72–75
27. J.C. Viala, P. Fortier, G. Claveyrolas, H. Vincent, and J. Bouix, Effect of Magnesium on the Composition, Microstructure and Mechanical Properties of Carbon Fibres, *J. Mater. Sci.*, 1991, **26**, p 4977–4984
28. J.C. Viala, G. Claveyrolas, F. Bosselet, and J. Bouix, The Chemical Behaviour of Carbon Fibres in Magnesium Base Mg-Al Alloys, *J. Mater. Sci.*, 2000, **35**, p 1813–1825
29. M. Russell-Stevens, R. Todd, and M. Papakyriacou, Microstructural Analysis of a Carbon Fibre Reinforced AZ91D Magnesium Alloy Composite, *Surf. Interface Anal.*, 2005, **37**, p 336–342
30. C. Sole, N.E. Drewett, and L.J. Hardwick, In Situ Raman Study of Lithium-Ion Intercalation into Microcrystalline Graphite, *Faraday Discuss.*, 2014, **172**, p 223
31. M.V. Kral, B.C. Muddle, and J.F. Nie, Crystallography of the bcc/hcp Transformation in a Mg–8Li alloy, *Mater. Sci. Eng. A*, 2007, **460–461**, p 227–232
32. U. Ruschewitz and R. Pottgen, Structural Phase Transition in Li_2C_2, *Z. Anorg. Allg. Chem.*, 1999, **625**, p 1599–1603
33. J. He, X. Song, W. Xu, Y. Zhou, M. Seyring, and M. Rettenmayr, Preparation and Phase Stability of Nanocrystalline Li_2C_2 Alloy, *Mater. Lett.*, 2013, **94**, p 176–178
34. R. Wang, X.Q. Yu, J.N. Bai, H. Li, X.J. Huang, L.Q. Chen, and X. Yang, Electrochemical Decomposition of Li_2CO_3 in NiO-Li_2CO_3 Nanocomposite Thin Film and Powder Electrodes, *J. Power Sources*, 2012, **218**, p 113–118
35. A. Moutinho, T. Lombardo, S. Kulmala, and A.C. Ferrari, Quantifying Defects in Graphene Via Raman Spectroscopy at Different Excitation Energies, *Nano Lett.*, 2011, **11**, p 3190–3196